Extended Design Space of Silicon-on-Nothing MEMS

Yu-Po Wong, Simón Lorenzo, Yu Miao, Jeremy Bregman, and Olav Solgaard, *Fellow, IEEE*

***Abstract*— Complex monolithic Si MEMS can be created using a single mask by extending the empty-space-in-silicon (ESS) or silicon-on-nothing (SON) technology. The fabrication combines isotropic and anisotropic etching with selective removal of passivation layers followed by hydrogen annealing. The resulting expanded design space includes multilayer structures and embedded cavities. The MEMS formation by the hydrogen annealing is simulated both at large scales and microscopic scales that together predict the shape of the finished MEMS. We demonstrate the accuracy of our process and simulations by fabricating single- and double-layer evacuated silicon voids that form Fabry-Perot optical pressure sensors with the sealed voids as pressure references. We also create multi-layered sensors with an integrated photonic crystals sensing diaphragm for improved optical readout. The sensors have a calculated 6.7 μV/Pa sensitivity and low noise over a dynamic range of over 70.9 kPa. [2019-0091]**

***Index Terms*— Silicon-on-nothing, photonic crystals, fiber sensor.**

I. Introduction

MEMS pressure sensors are widely used, and fiber-optical readout is preferred in many applications due to its immunity to electromagnetic interference and suitability for remote sensing [1], [2]. To achieve high resolution pressure sensing in a small formfactor with low-cost fabrication, it is desirable to create monolithic structures to avoid multi-material sensors that exhibit high temperature sensitivity and long-term instability due to material stress and stress gradients. Monolithic Si sensors have been created by empty-space-in-silicon (ESS) technology [3] and the closely related silicon-on-nothing (SON) technology [4]. These technologies, and our extension, are all based on hydrogen annealing, in which Si is reflowed at high-temperature (900∼1100°C) and low-pressure (∼10 torr) in a hydrogen environment. This process reshapes silicon by surface diffusion, and it is widely used to increase surface quality of silicon-based electronic and photonic devices [5]–[8].

Manuscript received April 20, 2019; revised June 29, 2019; accepted July 2, 2019. Date of publication July 26, 2019; date of current version October 1, 2019. This work was supported in part by the National Science Foundation Graduate Research Fellowship Program (NSF GRFP) under Grant DGE 1656518, in part by the Stanford Graduate Fellowship (SGF), in part by the Enhancing Diversity in Graduate Research Fellowship (EDGE), in part by the Boeing Company, and in part by the National Science Foundation under Award ECCS-1542152. Subject Editor G. Stemme. *(Corresponding author: Yu-Po Wong.)*

Y.-P. Wong is with the Department of Applied Physics, Stanford University, Stanford, CA 94305 USA (e-mail: mkenwong@gmail.com).

S. Lorenzo, Y. Miao, J. Bregman, and O. Solgaard are with the Department of Electrical Engineering, Stanford University, Stanford, CA 94305 USA.

Color versions of one or more of the figures in this article are available online at http://ieeexplore.ieee.org.

Digital Object Identifier 10.1109/JMEMS.2019.2927466

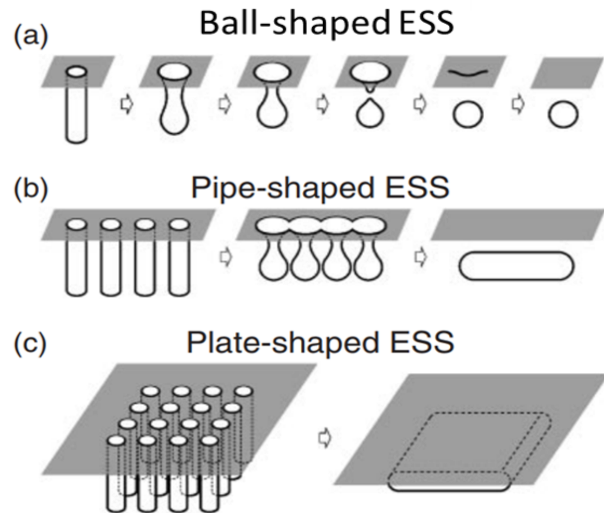

Fig. 1. Empty-space-in-silicon processes forming different geometries a) a ball, b) a pipe, and c) a plate. Reprinted with permission from [3]; ©2000 American Institute of Physics.

The ESS/SON processes can be used to create sealed cavities, or voids, inside bulk c-Si. Single-layer voids in the shape of balls, pipes, and plates can be produced as shown in Fig. 1. The diaphragms formed over plate-shaped cavities have been used as capacitive pressure sensors with metal electrodes added for electrical readout and have demonstrated good stability [9]. An important aspect of structures made by hydrogen annealing is that their vertical dimensions are controlled by etch depths, leading to better vertical control than other MEMS technologies, including structures based on Si-on-Insulator (SOI) materials.

In this paper, we describe a process that retains the advantages of ESS/SON, but offers more flexibility, larger design space, and the creation of more complex structures. This is achieved by introducing under-etching and selective removal of passivation layers, allowing multiple layers of voids to be fabricated using a single mask. We demonstrate this capability in simulations and experiments. Our sensor demonstrations use optical readouts, but electrical interfaces can be added.

II. GSON Process

Figure 2 shows how under-etching and selective removal of passivation layers can extend the design space by de-coupling the diaphragm and void thickness. The process (GSON) is a combination of the GOPhER process [10] and ESS/SON [11].

The standard one-layer GSON process follows these steps: 1) start with a standard silicon wafer, 2) thermal oxidation,

This work is licensed under a Creative Commons Attribution 4.0 License. For more information, see http://creativecommons.org/licenses/by/4.0/

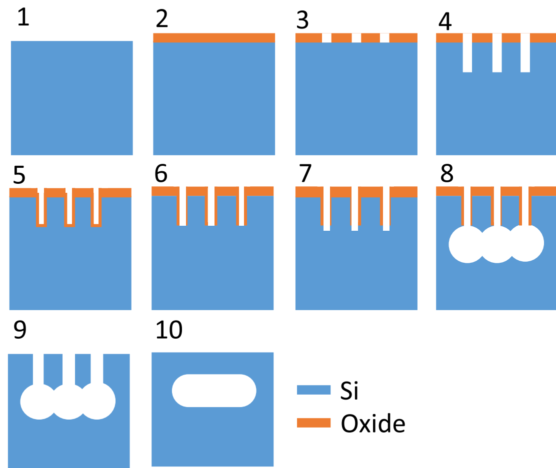

Fig. 2. Single layer GSON process.

3) pattern and etch trenches on an oxide film with CHF_3 chemistry, 4) etch directionally into silicon with a reactive ion etch (RIE) with HBr chemistry, 5) thermal oxidation for side wall protection, 6) etch directionally by RIE with CHF_3 chemistry to remove oxide at the bottom of the holes, 7) etch deeper into silicon by RIE with HBr chemistry, 8) undercut the top layer by isotropic silicon etch with SF_6 chemistry, 9) strip oxide with a hydrofluoric acid (HF) wet etch, 10) hydrogen anneal.

Just as important as the extended design space, is the capability of GSON process to create multiple-layer MEMS as shown in Fig. 3 using only a single mask. This two-layer process follows the steps of the standard process until step 8. To create the second structural layer, steps 4 to 8 are repeated (9-13). In the example shown in Fig. 3, the second layer has larger, connected spherical holes to create a plate shaped void after hydrogen annealing. The process is completed by etching in vapor hydrofluoric acid (HF) to remove all oxide (14), and the key step, hydrogen annealing, that transforms the structure to its final form (15). In this particular example, the first layer forms a Photonic Crystal of near spherical voids and the second layer is a plate-shaped void to act as an absolute pressure sensor.

III. Hydrogen Annealing Simulation

The shape evolution of hydrogen annealing is governed by surface diffusion that minimizes the surface energy. We simulate separately two regimes of this evolution: the macroscopic regime involving the formation of the overall cavity geometry and the microscopic regime involving the formation of the individual crystalline surfaces. For a full simulation, we first study a single unit cell in the macroscopic regime. Once it is topologically stable, i.e. not splitting or merging voids, we study the microscopic development.

IV. Macroscopic Regime

Macroscopic evolution is described by the Mullins surface diffusion equation:

$$v_n = B\frac{\partial^2 \kappa}{\partial s^2}, \quad (1)$$

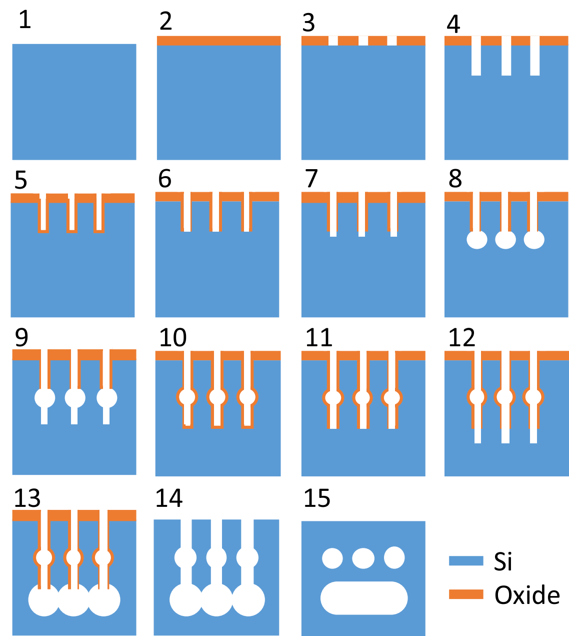

Fig. 3. Process flow for double layer MEMS structures.

where v_n is the migration velocity normal to the surface, B is the migration rate coefficient dependent on material and annealing condition, κ is the curvature, and $\frac{\partial^2 \kappa}{\partial s^2}$ is the surface Laplacian of the mean surface curvature.

In the macroscopic regime, a level-set method is used [12]–[14]. This method represents the surface as a set: $\Gamma = \{x, t|\varphi(x, t) = 0\}$, and the curvature can be calculated by:

$$\kappa = \nabla \cdot \frac{\nabla \varphi}{|\nabla \varphi|}, \quad (2)$$

where $\nabla\cdot$ is the divergence.

Note that κ is a second order term and v_n is a fourth order term. The migration is updated as:

$$\frac{\partial \varphi}{\partial t} + v_n |\nabla \varphi| = 0. \quad (3)$$

In order to do a stable numerical calculation on this fourth order partial differential equation, a velocity extension [15] is applied. This simulation is based on the code from R. Kant's thesis [16] and the Level-set Tool box [17].

A simulated shape evolution of a single cell of a silicon structure is shown in Fig. 4. The lateral boundary is set with a periodic boundary condition (PBC). The time unit in the annealing simulation is based on the migration rate coefficient, but it is not critical for the structures we are studying, because they are annealed to their equilibrium state. Fabrication of structures that are not at their annealed equilibrium will require precise determination of the migration rate coefficient. This has to be done experimentally. For the simulation shown in Fig. 4, the structures before and after annealing are described in Table 1.

A. Microscopic Regime

Microscopic simulations are used to study the formation of crystalline surfaces in the voids. The following equations

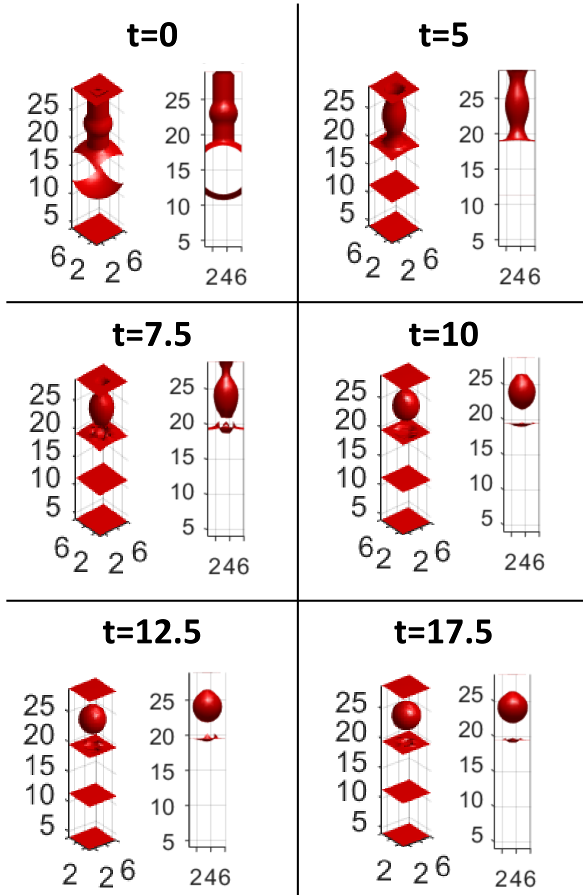

Fig. 4. Macroscopic hydrogen annealing simulation of a single cell. Time unit: arbitrary unit. Spatial unit: 200nm. Left: isometric view. Right: x-z plane view.

TABLE I
DIMENSIONS FOR ANNEALING SIMULATION IN FIG. 4

Physical Description	Value
Initial geometry	
Pitch	1.1 µm
PC hole diameter	600 nm
First ball radius	400 nm
Second ball radius	860 nm
First ball depth	1.2 µm
Second ball depth	2.8 µm
Anneal equilibrium state	
Diaphragm thickness	1.72 µm
Void thickness	1.70 µm
Ball radius	340 nm
Ball depth	766 nm

in this section is from the work by Sudoh *et al.* [4]. The microscopic evolution is modeled by the mean chemical potential for each crystalline facet:

$$\mu_i = \mu_0 + \Omega K_i, \tag{4}$$

where μ_i is the mean chemical potential of the i$^{\text{th}}$ facet, μ_0 is the bulk chemical potential, Ω is the single atom volume, and is the weighted mean curvature of the i$^{\text{th}}$ facet defined in [4].

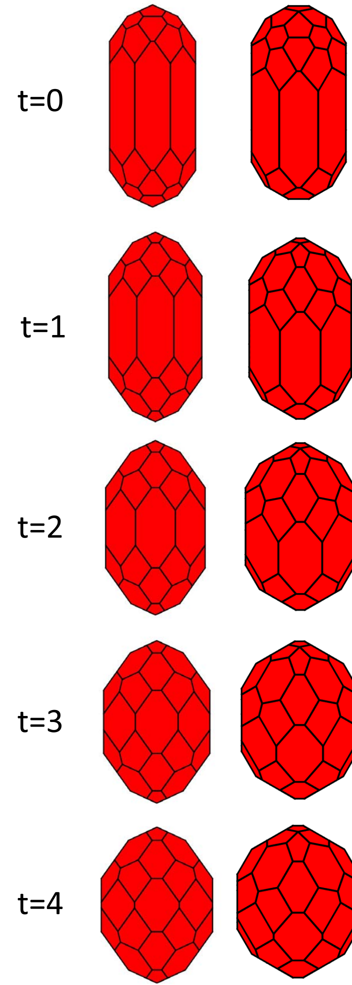

Fig. 5. Microscopic hydrogen annealing simulation of a single cell. Time unit: arbitrary unit. Left: view from [110] direction. Right: view from [111] direction.

Adatom flux between facets can be modeled from the mean chemical potential as:

$$J_{ij} = \frac{Dc_0}{kT}\frac{\mu_i - \mu_j}{\Delta x_{ij}}, \tag{5}$$

where J_{ij} is the adatom flux from j$^{\text{th}}$ facet into i$^{\text{th}}$ facet, D is the diffusion coefficient for the surface diffusion, c_0 is the equilibrium adatom concentration for a surface with zero curvature, k is the Boltzmann constant, T is the temperature, $\Delta x_{ij} = \sqrt{S}_i + \sqrt{S}_j$ is the estimation of the diffusion distance between facets, and S_i is the area of the facet. Finally, the normal velocity of each facet can be calculated by:

$$v_i = \frac{\Omega}{S_i}\sum_j l_{ij} J_{ij}, \tag{6}$$

where the summation sums over all the neighboring facets, and l_{ij} is the length of the intersection between facet i and facet j. Further details are described in [4].

The results of a microscopic annealing simulation are shown in Fig. 5. This simulation is an effective method for studying the facet shape evolution and for determining the crystalline surfaces of the equilibrium state.

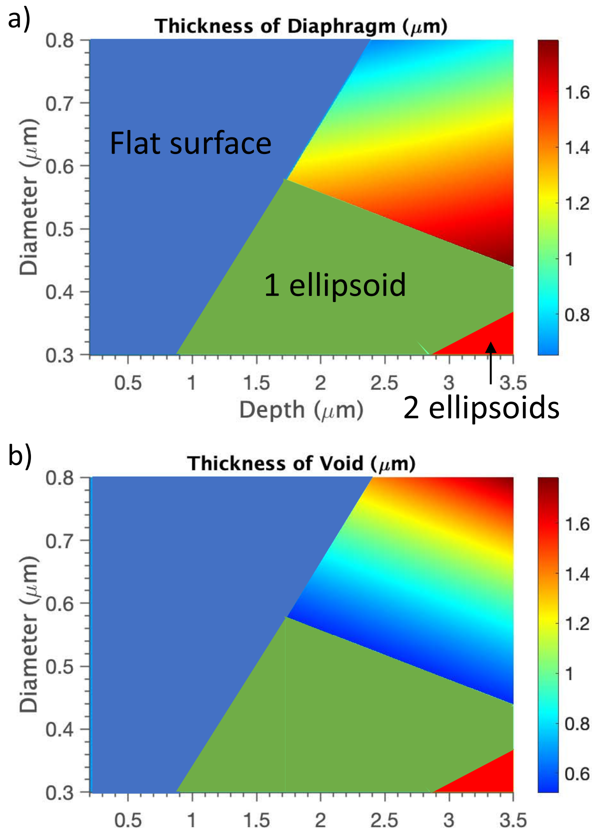

Fig. 6. Design space of the standard silicon-on-nothing process. Flat surface without structure, 1 ellipsoid and 2 ellipsoids are shown in both plot of design space. The thickness of diaphragm (a) and void layer (b) are plotted in the design space area for SON structure.

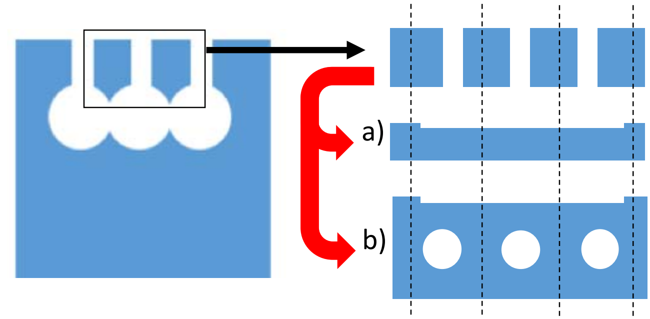

Fig. 7. Hydrogen annealing in the GSON process. The top layer is approximated (black arrow) as a free-standing diaphragm with an array of holes. After annealing of the diaphragm (red arrow), the final structure can be open/unstable, simple diaphragm (a), or diaphragm with ellipsoidal voids (b).

B. Design Space of SON Process

Sato *et al.* experimentally studied hydrogen annealing in the standard ESS/SON process using arrays of cylindrical holes [18] and developed empirical equations to relate the structural geometry before and after the annealing process. In our studies, we combine these empirical equations with numerical simulations to map a wider range of the design space. The three parameters that define the initial arrays of cylindrical holes are pitch (p), hole diameter (d), and hole depth (t).

The key result of the ESS/SON studies on cylindrical hole arrays is that the final structure after hydrogen annealing depends only on the initial relative shapes. Absolute dimensions only affect the time needed to reach the final equilibrium state. With this in mind, we set the period of the square array of cylindrical holes to 1 μm, and chose practical ranges for hole diameters and depths. The evolution of other sizes can then be inferred by scaling all three dimensions linearly. To stay within practically achievable lithography limits, we set the minimum hole diameters at 300 nm. Maximum hole diameter is set at 800 nm to avoid divergence in numerical simulation. The hole depth is up to a maximum of 3.5 μm, given by the achievable aspect ratio of typical reactive-ion etch (RIE) etch tools.

The results of the design space study show how the four different geometrical outcomes of hydrogen annealing depend on the starting geometry (Fig. 6a):

1. ***Flat surface:*** Low aspect ratios (t/d<3.0) make the holes disappear and leave flat and smooth surfaces.
2. ***Single ellipsoid:*** Small hole diameters and medium aspect ratios (3<t/d<9.5) transform the holes into sealed ellipsoids that don't connect to nearest neighbors.
3. ***Double ellipsoid:*** Small hole diameters and high aspect ratios (t/d>9.5), transform each hole into two ellipsoids that don't connect to nearest neighbors.
4. ***Plate-shaped void:*** Large hole diameters and high aspect ratios, transform the holes into ellipsoids that connect to nearest neighbor, creating a plate-shaped void.

Pitch, hole diameter, and hole depth are all critical parameters in the structure formation. The ratio between depth and diameter determines the number of ellipsoids in vertical direction. The ratio between pitch and diameter determines whether the ellipsoids connect into plate-shaped void.

In Fig. 6 (a) and (b), we describe the possible geometries of the plate-shaped voids when starting with arrays of holes on a 1μm pitc. The diaphragm thickness ranges from 0.67 μm to 1.76 μm, while the void thickness ranges from 0.54 μm to 1.75 μm. These two geometrical dimensions are not independent and show a strong negative correlation which severely limits the available design space.

In contrast, our GSON process does not limit the void thickness, because the under etching (steps 7 and 8 in Fig. 2) can be extended through a combination of RIE and isotropic etching, which can be deeper than μm. The thickness of the diaphragm will be limited, however, because at a given depth, the cylindrical holes will lead to the formation of spherical voids. To explore these limits, we model hydrogen annealing of free-standing diaphragms with two-dimensional arrays of cylindrical holes as shown in Fig. 7. As before, all dimensions scale linearly with the pitch, which is set to 1 um.

In the simulations, we vary the hole diameter and thickness of the initial diaphragm. The diaphragm thickness is given by: $t_{pc} = d_{etch} - r_{iso}$, where d_{etch} is the anisotropic silicon etch depth in the GOPhER process and r_{iso} is the radius of the isotropic etch in the GOPhER process. The results (Fig. 8) show the three different geometrical outcomes:

1. ***Open:*** A low aspect ratio (t/d<1.0) yields an open structure as there is not enough material to seal the diaphragm.

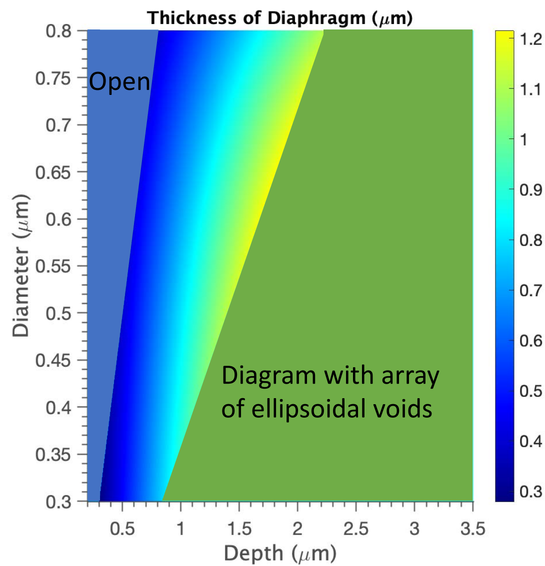

Fig. 8. Design space for the GSON process. Open unsealed structure and diaphragm with array of ellipsoidal voids are shown in design space. Thickness of diaphragm is plotted in the design space of diaphragm structure.

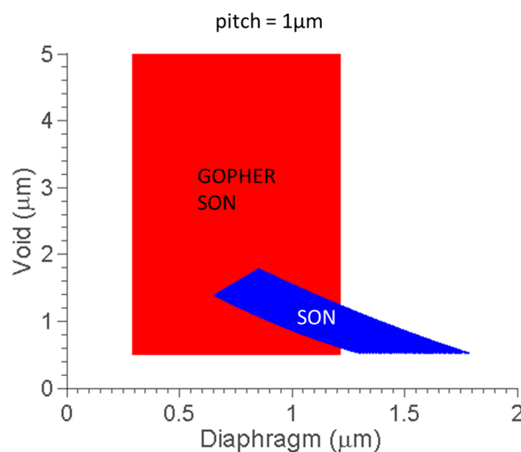

Fig. 9. Comparison of design spaces for the standard SON and GSON processes.

2. ***Diaphragm:*** Medium aspect ratios (1.0<t/d<2.8) yield continuous uniform diaphragms over a plate-shaped void.
3. ***Diaphragm with array of ellipsoidal voids:*** High aspect ratios (t/d>2.8) yield a diaphragm with ellipsoidal voids.

The final design spaces of the two processes are compared in Fig. 9. The voids can be extended to arbitrary thicknesses in the GSON process, so in this dimension, the new process provides a clear advantage. The diaphragm thickness ranges from 0.3 μm to 1.2 μm inGSON, while the standard process gives thicker diaphragms from of 0.67μm to 1.76μm for the same 1 um pitc. For the same lithography resolution limit, GSON process can give us thinner diaphragms, which leads to higher sensitivity.

C. Sensor Design, Fabrication and Characterization

To experimentally demonstrate the benefits of the GSON process, we developed three different MEMS structures.

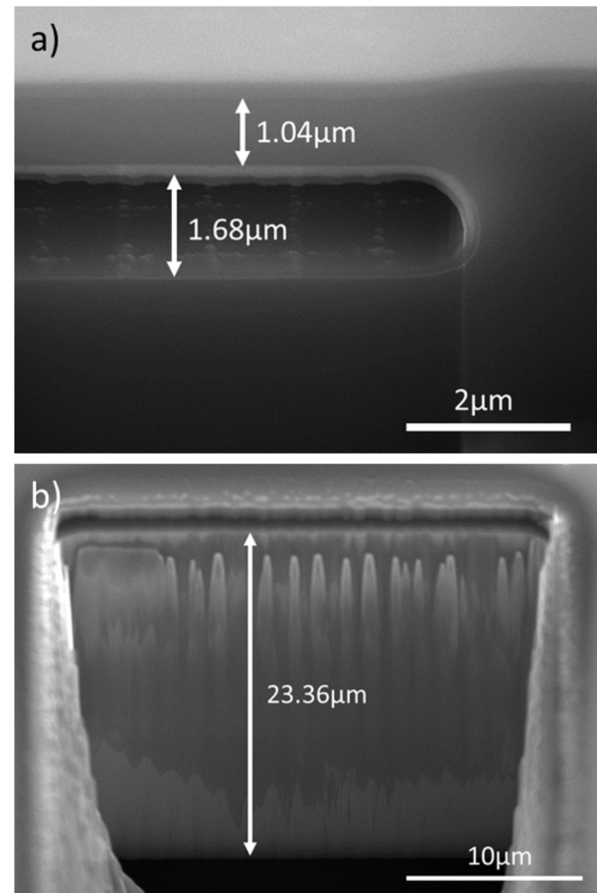

Fig. 10. SEMs taken at 52° view angle of a single crystalline pressure sensor fabricated by process shown in Fig. 2: a) edge of the SON structure. b) thinned substrate. A Focused Ion Beam (FIB) has been used to cut the wafer to reveal the structure. The FIB leaves residue that can be observed in the SEMs.

The first is an absolute pressure sensor fabricated in the one-layer GSON process (Fig. 2) and designed to have a nearly circular top diaphragm. The photolithography mask has an array of holes with a 1 μm pitch arranged in a circular array 100μm in diameter. The structure before hydrogen annealing has a diaphragm thickness of ~1.6 μm and etched hole diameters of ~650 nm (Fig. 7). The hydrogen annealing equipment is Centura Epi from Applied Materials. The temperature of annealing process is 1100°C and lasts for 10 minutes. The process pressure is 10 Torr and hydrogen flow rate is 5 SLM.

After completion of the standard GSON process, LPCVD low-stress silicon nitride is deposited as a hard mask and patterned on the backside of the wafer, and a carefully-timed KOH etch without an etch stop is used to thin the wafer underneath the sensors for fiber-optic access. The backside of the sensor is designed to be thick enough to negate mechanical displacement under pressure. However, excessive thickness causes optical coupling loss between the fiber and the device, reducing the overall signal amplitude. We therefore time the KOH etch step to yield backsides approximately 20 μm thick (Fig. 10 b).

Cross sections at this stage in the processing are shown in Fig. 10. All measured lengths are compensated for the viewing angle. The diaphragm is uniform with a thickness

TABLE II
PRESSURE SENSOR DEVICE DIMENSIONS

Physical Description	Value
Diaphragm diameter	100 μm
Diaphragm thickness	1.04 μm
Void thickness	1.68 μm
Backside thickness	23.36 μm
Chromium coating	5 nm
Gold coating	40 nm

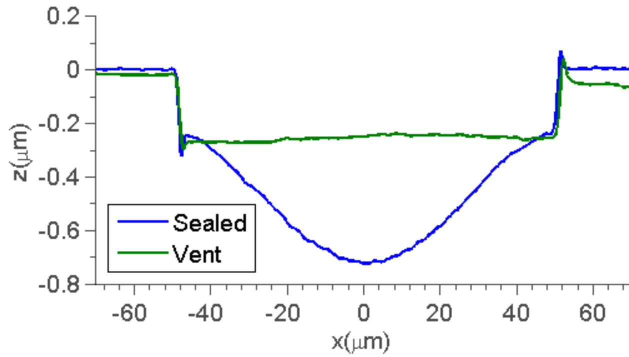

Fig. 11. Optical profiler measurement for the SON structure.

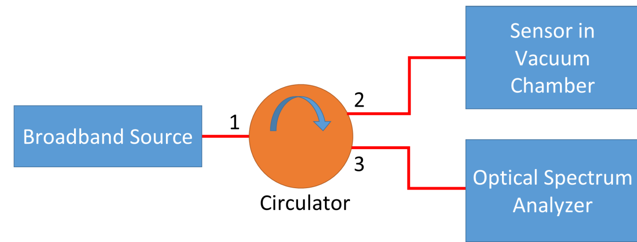

Fig. 12. Experimental setup for pressure sensor testing.

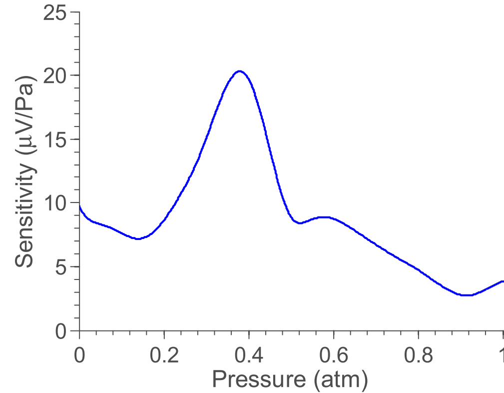

Fig. 13. The sensitivity of our pressure sensor is above 6.7 μV/Pa for pressures up to 0.7 atm (=70.9 kPa), and above 2.7 μV/Pa for pressures up to 1 atm (101 kPa).

of 1.04 μm, and the void layer is 1.68 μm thic (Fig. 10a), while the substrate under the SON structure is thinned to 23.36μm (Fig. 10b). The fabrication is completed by evaporating 5 nm of chromium and 40 nm of gold onto the top surface to enhance reflectivity. The dimensions of the final device are summarized in Table 2. Using the GSON process design map of Fig. 8 and the measured structural dimensions before annealing, we estimated the diaphragm thickness after annealing to be ~1.03 μm. This agrees well with the 1.04 μm measured thickness.

After cooling down to room-temperature, the sealed voids in the GSON sensors are at low pressure (~2.1 Torr = 280Pa). This pressure value is calculated from equipment pressure at the end of the annealing process. When the device is at room-temperature and standard atmospheric pressure, the pressure difference between two sides of the diaphragm bends the diaphragm inward. To characterize this deflection, we tested the surface profile of the diaphragm with an optical profiler under two different conditions: atmospheric pressure and zero differential pressure due to a vent hole cut into the diaphragm using a Focused Ion Beam (FIB). These surface profiles are shown in Fig. 11. With the vent hole, there is no applied differential pressure across the diaphragm, but the diaphragm remains recessed by 225 ±31 nm. This is due to the silicon reflowing to fill and seal the etched holes. When the device is under atmospheric pressure, the center of the diaphragm is 0.727 ±0.004 μm elow the wafer surface, which means the diaphragm center deflects 0.472±0.010μm. This measured displacement is close to the 0.50μm displacement predicted by COMSOL simulatios.

We assemble the sensor chip with a single-mode fiber (Corning model#: SMF-28e+) to create a fiber-tip pressure sensor that is calibrated in the set-up of Fig. 12. The vacuum chamber used for the experiment includes a pump port, a vent port, a pressure gauge, and a fiber feedthrough for fiber-based interrogation. With the pressure sensor in the chamber, the fiber is connected to the optical system. It consists of a broadband source, a fiber circulator, and an optical spectrum analyzer that collects reflectivity spectra of the sensor under different pressures.

Using two wavelengths to interrogate the sensor, we can uniquely determine pressure with excellent sensitivity. The sensitivity is defined as the gradient of output over pressure. In our case, the output is the voltage signal from the photodiode. We show the combined sensitivity of interrogating the sensor at both 1548 nm and 1550 nm wavelengths (Fig. 13). The sensitivity at all wavelengths is affected by the nonlinear mechanical displacement of the diaphragm. This causes reduced sensitivity at high pressures. The sensitivity of a single wavelength is proportional to the derivative of its Fabry-Perot spectrum. Each wavelength has distinct pressure regions with large spectral derivatives. By combining these regions from 0 to 1 atm, we maximize sensitivity and the sensor's dynamic range (Fig. 13). Both wavelengths have high sensitivity near ~0.4 atm, resulting in the peak of Fig. 13.

To demonstrate the capability of GSON to create multiple-layers of MEMS structures, we fabricated absolute pressure sensors with integrated photonic crystal (PC) mirrors, following the process described in Fig. 3 [11]. The macroscopic annealing simulation of this device is shown in Fig. 4, and the SEM image of the device is shown in Fig. 14. The oxide passivation layers of the GSON process successfully protect the hole sidewalls during the isotropic etch steps.

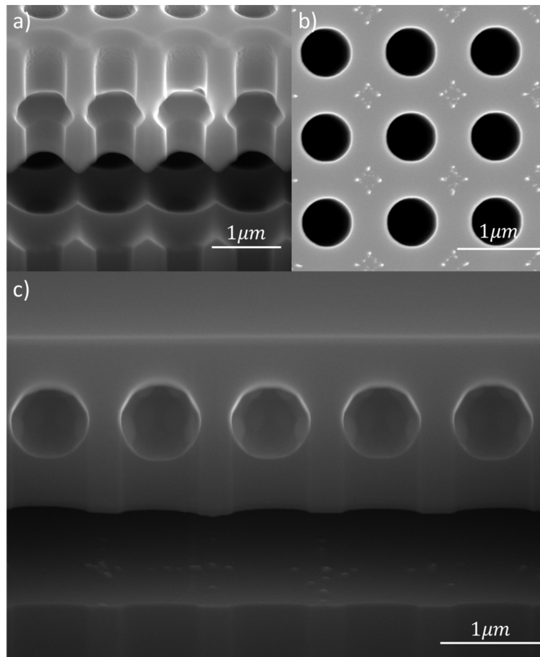

Fig. 14. SEMs of a double GSON process (Fig. 3): a) 52° tilted SEM image before annealing. b) Top view SEM image before annealing. The diamond-shape marks are residue from oxide strip by vapor HF [19], which was not completely removed before imaging but properly removed before annealing. c) 52° tilted SEM image after annealing. Reprinted with permission from [11].

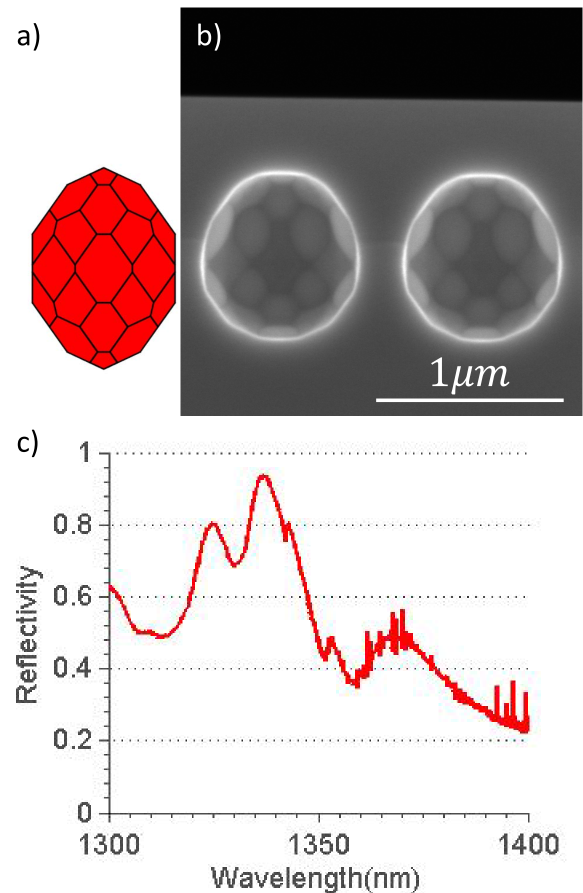

Fig. 15. a) Simulated equilibrium state from Fig.5, b) cross-section of PC mirror created by arrays of voids, c) measured reflectivity profile. Reprinted with permission from [11].

The preserved sidewalls, shown after oxide removal in Fig. 14a, are vital to the successful formation multiple-layer structures. The details of the etch profiles will, however, lead to discrepancies between the experiments and simulations as discussed below.

From Fig. 14c, the dimensions after annealing are: diaphragm thickness = 2.2 μm, void thickness = 1.21 μm, ball radius = 440 nm, ball depth = 1 μm. These values deviate from the simulation results in Table 1. This can be explained by two imperfections in the simulation: 1) the macroscopic simulation does not consider the microscopic crystalline surfaces on integrated PC. 2) the complex etching profile of isotropic silicon etches isn't captured by the simple geometry used in the simulation.

The array of ellipsoidal voids in the diaphragm creates a high reflectivity PC mirror [20], [21] that removes the need for metallization to increase reflectivity as was done in the single MEMS layer pressure sensor. We used the microscopic hydrogen annealing simulations (Fig. 5) to calculate the detailed shape of the ellipsoidal voids. We compare these simulations in Fig. 15a to the fabricated structures in Fig. 15b, and see that the simulations predict the outcome with very good precision. There are some differences caused by gravity during annealing, which is not included in the simulation model.

The crystalline quality of hydrogen annealed Si has been reported in the literature [4]. It has no detectable stress by Raman measurement, no defects by transmission electron microscopy (TEM), and similar roughness as standard silicon wafers [4]. For our sample, we demonstrated that the crystalline surfaces formed on integrated PC during annealing agree with those of single-crystalline silicon (Fig. 15ab), indicating that the membrane has largely returned to the single-crystalline state. For mechanical properties, bending of the diaphragm under pressure agrees with model using crystalline silicon mechanical properties. The diaphragm should therefore have similar mechanical properties to single-crystalline silicon.

The measured reflection spectrum of the PC mirrors in Fig. 15c shows that we achieve reflectivity over 90% over a $\sim$10 nm range close to 1340 nm wavelength.

We characterized the pressure sensor with the integrated PC mirror using the two different fiber configurations shown in Fig. 16a and b. For the first method, we collimated light from a SMF-28 fiber using a fiber collimator with a 2 mm focal length. We then used the resulting Gaussian beam, with an 80μm FWHM, to directly read the reflectivity of the device at different pressures. The result is shown in Fig. 16 (c) where we see high reflectivity between 1530 nm and 1570 nm at low pressure, demonstrating the high reflectivity of the PC mirror. Resonances from PC mirrors can be seen at 1571 nm and 1584 nm. The reflectivity drops with increasing pressure, due to the increasing beam clipping as the diaphragm surface curves under increasing differential pressure.

We then coated a SMF-28 fiber with 15 nm of gold and positioned it 65 μm above the sensor without a collimator to perform Fabry-Perot sensing. In Fig. 16 (d), we see a

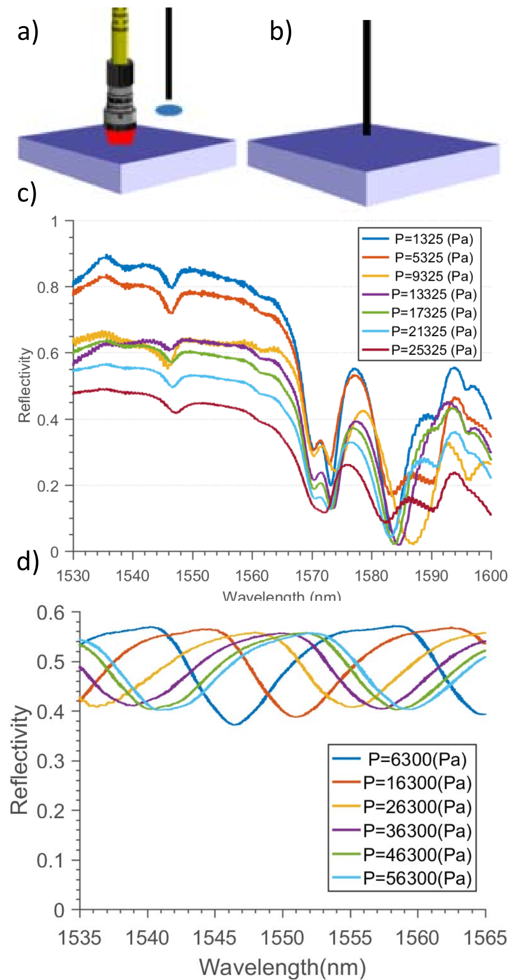

Fig. 16. Experimental setups and results for free-space testing of a GSON device with an integrated PC mirror. a) setup for reflectivity. b) setup for Fabry-Perot spectra. c) reflectivity spectra. d) Fabry-Perot spectra.

red-shifting of the Fabry-Perot spectra with increasing pressure. This corresponds to the cavity length increasing under increasing pressure.

We expect a smaller functional pressure range for this PC mirror sensor as the fabricated void layer is thinner. There is therefore less space for the diaphragm to displace into before touching down.

V. Conclusion

Monolithic Si MEMS created by SON/ESS processes have numerous advantages due to the excellent mechanical, electrical, thermal, and chemical properties of Si. By adding selective removal of passivation and isotropic under etch as in the GSON process, the design space for monolithic Si MEMS is extended and complex, multilayered structures can be created using a single lithography step. The key process step, hydrogen annealing, can be precisely modeled both on the macroscopic level and down to the details of appearance of crystalline planes in voids. The simulations therefore allow detailed predictions of the outcomes of complex designs. In this paper the experimental focus is on pressure sensors with optical readout. We demonstrate both simple pressure sensing diaphragms over reference cavities and more complex structures with integrated Photonic Crystal mirrors in the diaphragms to enhance reflectivity. Both sensors are miniaturized with sensing diaphragms approximately 100 μm in diameter and 1 μm in thickness, and both exhibit excellent sensitivity and stability. These sensors are examples of the types of structures that can be created using the GSON process with a single mask. With additional lithography steps, the GSON process can be used for a wide range of MEMS, including electrical sensors, actuators and resonators.

Acknowledgment

Part of this work was performed at the Stanford Nano Shared Facilities (SNSF)/Stanford Nanofabrication Facility (SNF).

References

[1] D. C. Abeysinghe, S. Dasgupta, H. E. Jackson, and J. T. Boyd, "Novel MEMS pressure and temperature sensors fabricated on optical fibers," *J. Micromech. Microeng.*, vol. 12, no. 3, pp. 229–235, 2002.
[2] X. Wu, C. Jan, and O. Solgaard, "Monolithic photonic crystal-based fiber-tip Fabry–Pérot static pressure sensor," in *Proc. Int. Conf. Opt. MEMS Nanophoton. (OMN)*, Aug. 2013, pp. 49–50.
[3] I. Mizushima, T. Sato, S. Taniguchi, and Y. Tsunashima, "Empty-space-in-silicon technique for fabricating a silicon-on-nothing structure," *Appl. Phys. Lett.*, vol. 77, no. 20, pp. 3290–3292, 2000.
[4] K. Sudoh, H. Iwasaki, R. Hiruta, H. Kuribayashi, and R. Shimizu, "Void shape evolution and formation of silicon-on-nothing structures during hydrogen annealing of hole arrays on Si(001)," *J. Appl. Phy.*, vol. 105, Mar. 2009, Art. no. 083536.
[5] N. Sato and T. Yonehara, "Hydrogen annealed silicon-on-insulator," *Appl. Phys. Lett.*, vol. 65, no. 15, pp. 1924–1926, Oct. 1994.
[6] H. Moriceau, A. M. Cartier, and B. Aspar, "Hydrogen annealing treatment used to obtain high quality SOI surfaces," in *Proc. IEEE Int. SOI Conf.*, Oct. 1998, pp. 37–38.
[7] J.-S. Lee, Y.-K. Choi, D. Ha, S. Balasubramanian, T.-J. King, and J. Bokor, "Hydrogen annealing effect on DC and low-frequency noise characteristics in CMOS FinFETs," *IEEE Electron Device Lett.*, vol. 24, no. 3, pp. 186–188, Mar. 2003.
[8] M.-C. M. Lee and M. C. Wu, "Thermal annealing in hydrogen for 3-D profile transformation on silicon-on-insulator and sidewall roughness reduction," *J. Microelectromech. Syst.*, vol. 15, no. 2, pp. 338–343, Apr. 2006.
[9] X. Hao *et al.*, "Application of silicon on nothing structure for developing a novel capacitive absolute pressure sensor," *IEEE Sensors J.*, vol. 14, no. 3, pp. 808–815, Mar. 2014.
[10] S. Hadzialic, S. Kim, A. S. Sudbo, and O. Solgaard, "Two-dimensional photonic crystals fabricated in monolithic single-crystal silicon," *IEEE Photon. Technol. Lett.*, vol. 22, no. 2, pp. 67–69, Jan. 15,2010.
[11] Y.-P. Wong, J. Bregman, and O. Solgaard, "Monolithic silicon-on-nothing photonic crystal pressure sensor," in *Proc. 19th Int. Conf. Solid-State Sens., Actuators Microsyst. (TRANSDUCERS)*, Jun. 2017, pp. 1963–1966.
[12] J. Sethian, *Level Set Methods and Fast Marching Methods: Evolving Interfaces in Computational Geometry, Fluid Mechanics, Computer Vision, and Materials Science*. Cambridge, U.K.: Cambridge Univ. Press, 1998.
[13] D. Chopp and J. A. Sethian, "Motion by intrinsic Laplacian of curvature," *Inter. Free Bound.*, vol. 1, no. 1, pp. 107–123, Jun. 1999.
[14] P. Smereka, "Semi-implicit level set methods for curvature and surface diffusion motion," *J. Sci. Comput.*, vol. 19, nos. 1–3, pp. 439–456, Dec. 2003.
[15] D. Adalsteinsson and J. A. Sethian, "The fast construction of extension velocities in level set methods," *J. Comput. Phys.*, vol. 148, no. 1, pp. 2–22, Jan. 1999.
[16] R. Kant, "Silicon migration as a process for micro/nanofabrication," Ph.D. dissertation, Dept. Elect. Eng., Stanford Univ., Stanford, CA, USA, 2009.
[17] I. M. Mitchell, "The flexible, extensible and efficient toolbox of level set methods," *J. Sci. Comput.*, vol. 35, nos. 2–3, pp. 300–329, 2008.
[18] T. Sato *et al.*, "Fabrication of silicon-on-nothing structure by substrate engineering using the empty-space-in-silicon formation technique," *Jpn. J. Appl. Phys.*, vol. 43, no. 1, pp. 12–18, 2004.

[19] R. J. Carter, J. R. Hauser, and R. J. Nemanich, “Surface residue island nucleation in anhydrous HF/Alcohol vapor processing of Si surfaces,” *J. Electrochem. Soc.*, vol. 147, no. 9, pp. 3512–3518, 2000.

[20] W. Suh, M. F. Yanik, O. Solgaard, and S. Fan, “Displacement-sensitive photonic crystal structures based on guided resonance in photonic crystal slabs,” *Appl. Phys. Lett.*, vol. 82, no. 13, pp. 1999–2001, 2003.

[21] O. Kilic *et al.*, “Photonic crystal slabs demonstrating strong broadband suppression of transmission in the presence of disorders,” *Opt. Lett.*, vol. 29, no. 23, pp. 2782–2784, 2004.

Yu-Po (Ken) Wong received the B.S. degree in physics and mathematics from Duke University in 2012, and the M.S. degree in electrical engineering and the Ph.D. degree in applied physics from Stanford University, in 2015 and 2018, respectively. His research focuses on fundamental properties of photonic crystal and fabrication and characterization of photonic crystal fiber-tip sensors. He is a member of the Optical Society of America.

Simón Lorenzo received the B.S. degree in physics with a minor in mathematics from Louisiana State University, Baton Rouge, LA, USA, in 2017, and the M.S. degree in electrical engineering from Stanford University, Stanford, CA, USA, in 2019, where he is currently pursuing the Ph.D. degree in electrical engineering. His research interests include optical device design and nanofabrication with a recent focus on photonic crystal fiber-tip sensors. He is a member of the Optical Society of America and a Membership Committee Chair of their student branch at Stanford University.

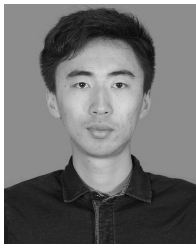

Yu Miao received the B.S. degree in electrical engineering from Tsinghua University, China, in 2015, and the M.S. degree in electrical engineering from Stanford University, USA, in 2018, where he is currently pursuing the Ph.D. degree in electrical engineering. His research interests include photonics, dielectric laser accelerators, optical MEMS, nanofabrication, and solar cells. His research is focus on dielectric laser accelerators.

Jeremy Bregman received the B.S. and M.S. degrees in electrical engineering from Stanford University, USA, in 2014 and 2016. He is currently a part of the R&D Team with Source Photonics, Los Angeles, delivering 400G PAM4 transceivers for the datacenter telecommunication market. While at Stanford, his research interests includes the design and fabrication of active optoelectronic components and Optical MEMS sensors. After Stanford, he began researching in the field of tactical and nav-grade MEMS components and photonic systems at HRL Laboratories.

Olav Solgaard (F’17) received the Ph.D. degree from Stanford University in 1992. His doctoral dissertation: Integrated Semiconductor Light Modulators for Fiber-optic and Display Applications was the basis for the establishment of a Silicon Valley firm Silicon Light Machines (SLM), co-founded by Dr. Solgaard in 1994.

From 1992 to 1995, he carried out research on optical MEMS as a Post-Doctoral Fellow with the University of California, Berkeley, and in 1995, he joined the Electrical Engineering Faculty of the University of California, Davis (UC Davis). His work at UC Davis led to the invention of the multi-wavelength, fiber-optical switch, which has been developed into commercial products by several companies. In 1999, he joined Stanford University, where he is currently a Professor of electrical engineering and the Director of Graduate Studies with the Department of Electrical Engineering. He has authored more than 370 technical publications and holds 75 patents. His research interests include optical MEMS, photonic crystals, optical sensors, microendoscopy, atomic force microscopy, and solar energy conversion.

Dr. Solgaard is a Fellow of the Optical Society of America, the Royal Norwegian Society of Sciences and Letters, and the Norwegian Academy of Technological Sciences.